Chemical Geology 608 (2022) 121040

Contents lists available at ScienceDirect

Chemical Geology

journal homepage: www.elsevier.com/locate/chemgeo

Radiogenic isotope record of magma genesis and lithospheric geodynamics of the Rukwa Rift Basin, Tanzania, from mid Mesozoic to present

L. Lawrence [a], C. Spandler [b,*], H.L. Hilbert-Wolf [a], C. Mtelela [c], N.J. Stevens [d,e], P.M. O'Connor [d,e], E.M. Roberts [a]

[a] Geosciences, James Cook University, Townsville, QLD 4811, Australia
[b] Department of Earth Sciences, The University of Adelaide, Adelaide, SA 5005, Australia
[c] Department of Geology, University of Dar es Salaam, P.O. Box 35052, Dar es Salaam, Tanzania
[d] Department of Biomedical Sciences, Ohio University Heritage College of Osteopathic Medicine, Athens, OH 45701, USA
[e] Ohio Center for Ecological and Evolutionary Studies, Ohio University, Athens, OH 45701, USA

ARTICLE INFO

Editor: Catherine Chauvel

Keywords:
Continental rift magmatism
East African Rift System
Western Branch
Rukwa
Sm-Nd isotopes
Enriched mantle

ABSTRACT

The Western Branch of the East African Rift System has experienced multiple episodes of basin development and intraplate alkaline volcanism since the Jurassic, however the geodynamic processes and lithospheric evolution involved in this protracted geological history remains poorly defined. Here, we present Sm-Nd, Lu-Hf, and Rb-Sr isotopic data of igneous minerals for three magmatic episodes that coincide with basin reactivation in the Rukwa Rift of southwestern Tanzania, respectively represented by: (1) the Jurassic to Cretaceous Panda Hill carbonatite; (2) the late Oligocene phonolitic-carbonatitic Nsungwe Formation tuffs; and (3) the Miocene–recent bi-modal volcanism of the Rungwe Volcanic Province. Of these, the Nsungwe Formation tuffs offer a discrete record of the early phases of lithospheric disturbance associated with modern rifting of the Western Branch.

Alkaline magmas erupted prior to the Miocene are isotopically distinct (εNd +0.5 to +1.5 and $^{87}Sr/^{86}Sr$ 0.7041) from modern Rungwe lavas and likely originate from a lithospheric mantle that experienced enrichment during the Pan-African Orogeny (~550–700 Ma). Consistent with previous studies, our results indicate that Rungwe Volcanic Province magmas were generated from a mixed, isotopically-enriched component of the lithospheric mantle that may have developed during the ca. 1.0 Ga Irumide Orogeny. The observed change in the source region of rift lavas though time is consistent with progressing melting of a compositionally layered lithosphere. Combined with existing geophysical and sedimentological data, we hypothesise that the lithosphere beneath the Rukwa-Malawi-Usangu junction of the Western Branch experienced an episode of destabilisation and foundering (lithospheric drip), during the early stages of East African Rift development.

1. Introduction

The interconnected tectonic basins, flanking escarpments and intraplate volcanism of the East African Rift System (EARS) serve as a natural laboratory for the study of active continental break-up. Over the past few decades, a key focus in this area has been linking deep geophysical observations of the lithospheric and deep mantle, with geochemical and isotopic data of rift lavas at the surface to discern lithospheric processes that govern continental break-up (Morley et al., 1992a; Furman and Graham, 1999; Nyblade, 2011; Castillo et al., 2014; Furman et al., 2016; Tepp et al., 2018; Rooney, 2020; Mesko, 2020). Given the vast spatial extent and temporal history of the EARS (>4000 km and > 40 m.y., respectively) and the diverse nature of rift lavas, discrepancies between models for the evolution of the sub-continental lithospheric mantle and product magmas are commonplace (Furman, 1995; Furman and Graham, 1999; Bagley and Nyblade, 2013; Castillo et al., 2014; Furman et al., 2016; Rooney, 2020). Nonetheless, some clarity is emerging with regards to the key ingredients involved in the formation and evolution of the EARS, and continental breakup more generally. These include; the presence and involvement of the African Large Low Shear Velocity Province (LLSVP), also referred to as the African Superplume (Pik et al., 2008; Nyblade, 2011; Bagley and Nyblade, 2013; Castillo et al., 2014); a significant reduction in northward motion of the African plate between 30 and 19 Ma (O'Connor et al., 1999); and inherited metasomatic

* Corresponding author.
E-mail address: carl.spandler@adelaide.edu.au (C. Spandler).

https://doi.org/10.1016/j.chemgeo.2022.121040
Received 7 March 2022; Received in revised form 2 July 2022; Accepted 21 July 2022
Available online 25 July 2022

heterogeneities (i.e. mantle metasomes) within the lithospheric mantle of eastern Africa (Ivanov et al., 1998; Rogers et al., 1998; Furman and Graham, 1999; Rooney, 2020).

The LLSVP is a deep mantle feature interpreted through a series of connected low-velocity seismic anomalies suggested to contribute both heat and material across the 660 km discontinuity beneath the entire EARS (Nyblade, 2011; Bagley and Nyblade, 2013; Castillo et al., 2014). Based on isotopic data, the LLSVP, termed "Plume-V" by Castillo et al. (2014), is implicated as a magma source for the Kivu, Virunga and Rungwe volcanic provinces in the Western Branch, and the Ethiopian and Kenyan rift lavas in the Eastern Branch (Halldórsson et al., 2014). The isotopic variability across and within sections of the EARS is suggested to be a function of degree of metasomatic overprint and/or mixing with locally heterogenous 'common lithospheric mantle' en-route to the surface (Furman and Graham, 1999; Bell and Tilton, 2001; Castillo et al., 2014; Furman et al., 2016; Rooney, 2020). The variably enriched 'common lithospheric mantle' as described by Furman and Graham (1999) broadly reflects a period of regional carbonatite metasomatism that impacted the lithospheric mantle beneath the EARS between ca. 1000 and 500 Ma.

One distinction often made between the Eastern and Western Branches of the EARS (Fig. 1A) is that magmatism in the Eastern Branch is in general older, more voluminous and less isotopically variable than the younger Western Branch, the latter of which hosts some of the most alkaline, silica-undersaturated and isotopically variable lavas recorded (Ebinger, 1989; Ivanov et al., 1998; Rogers et al., 1998; Furman and Graham, 1999; Rooney, 2020). An extensive orogenic history preserved along the southern and western margins of the Tanzanian Craton has been suggested to influence the geochemical character of lavas of the Western Branch (Fig. 1B; Rogers et al., 1998; Furman and Graham, 1999). Here, Proterozoic subduction-related metasomatic processes are implicated in the development of heterogeneities in the lithospheric mantle and the pronounced spatial and temporal isotopic variability within the Western volcanic provinces (Furman, 1995; Rogers et al., 1998; Furman and Graham, 1999; Rosenthal et al., 2009; Hudgins et al., 2015; Rooney, 2020). Poor preservation and scarcity of early rift lavas in surface outcrop has hampered efforts to uncover a complete magmatic history for the Western Rift segments. Additionally, the complex nature of the mantle lithosphere and restricted age range (<12 Ma) of most exposed magmatic rocks in this region has impeded modelling of the source region for Western Rift lavas (Furman, 1995; Rogers et al., 1998; Furman and Graham, 1999; Rosenthal et al., 2009; Foley et al., 2012; Castillo et al., 2014).

Advances in in-situ micro-analysis techniques now provide a convenient means to acquire isotopic records of magmatic rocks directly from igneous minerals, thereby avoiding issue of extensive weathering and alteration. Applying this approach to the poorly exposed and preserved volcanic rocks of the Western Branch provides an opportunity to expand the isotopic record of magmatism through time, and therefore better understand the spatial and temporal evolution of this segment of the EARS. In this work, we utilise Rb-Sr, Sm-Nd and Lu-Hf isotope chemistry of igneous minerals sourced from volcanic rocks in the Rukwa Rift Basin and the Rungwe Volcanic Province (Fig. 2) to establish the isotopic evolution of the magmatism in the Rukwa–Malawi–Usangu junction from ca. 165 Ma to the present. By linking the isotopic evolution of magmatism with existing geophysical and geological data, we evaluate the nature and composition of the local mantle lithosphere and present a conceptual tectono-magmatic model for the Mesozoic-recent history of the long-lived Rukwa Rift Basin. Such a model may have broader implications for the break-up of complex ancient terrains elsewhere, particularly along the Western Branch and southernmost Eastern Branch of the EARS.

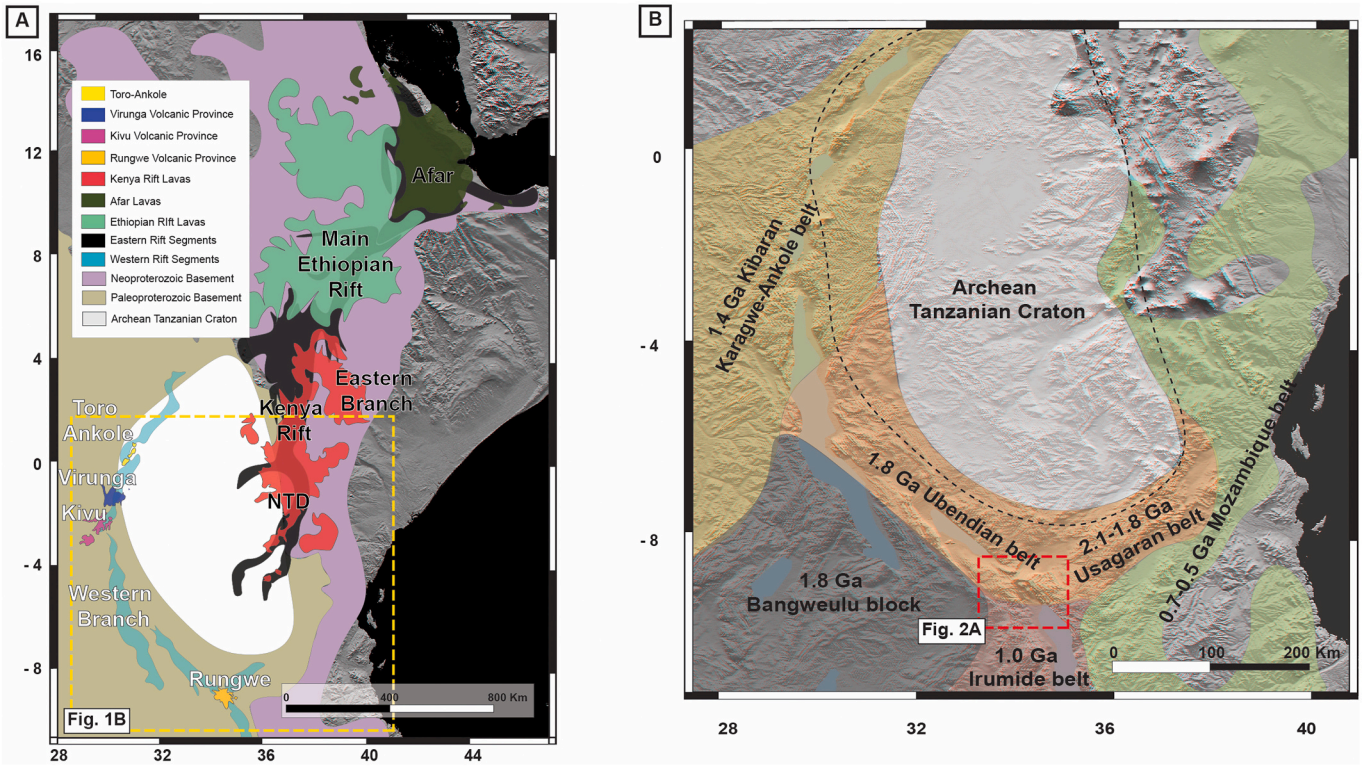

Fig. 1. A) Image of the EARS showing rift segments, basement geology and Cenozoic volcanic rocks as presented by Rooney (2020). The base image is modified from the NASA Shuttle Radar Topography Mission collection. The dashed yellow box indicates the area shown in Fig. 1B. B) Regional map showing the approximate ages and distribution of orogenic basement terranes surrounding the Tanzanian Craton (adapted from Roberts et al., 2012). The dashed red box indicates the area shown in Fig. 2A. (For interpretation of the references to colour in this figure legend, the reader is referred to the web version of this article.)

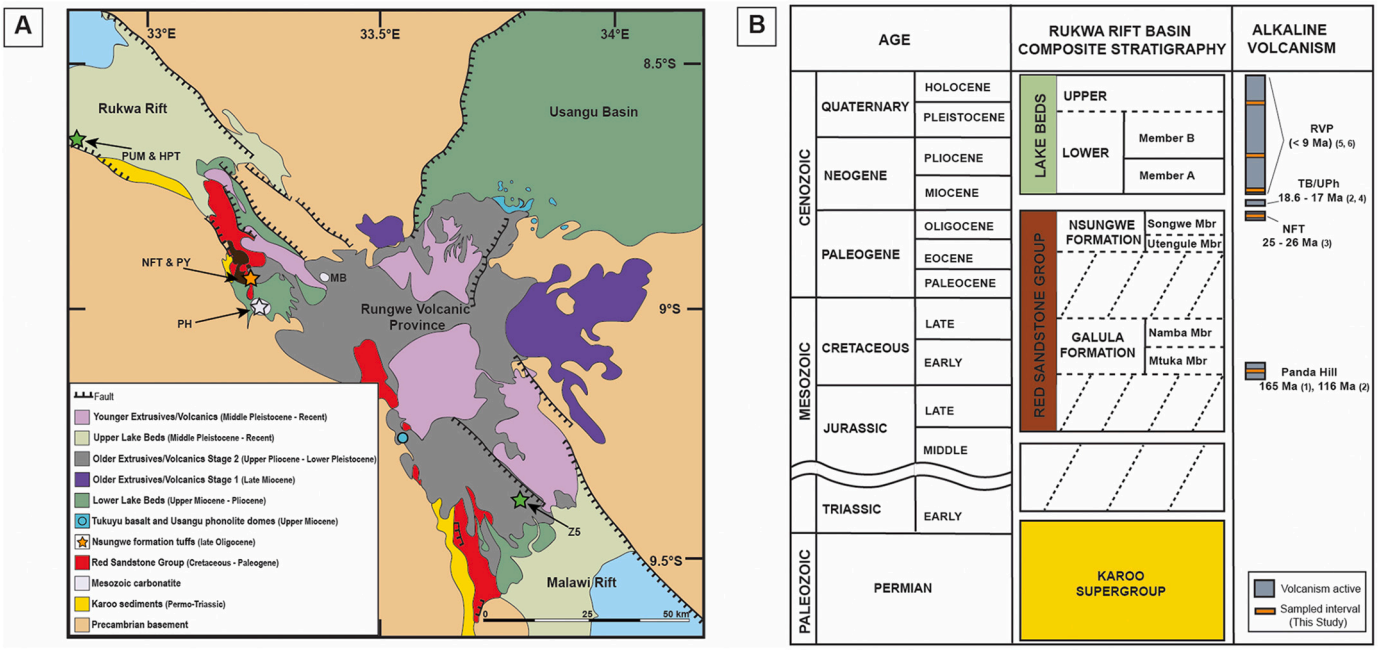

Fig. 2. A) Geological map of the Rukwa–Malawi–Usangu junction and Rungwe Volcanic Province adapted from Fontijn et al. (2012) and Rasskazov et al. (2003). The orange star marks the sample locality for the NFT and PY samples and the white star marks the location of Panda Hill carbonatite (sample PH). The green stars marks the sample locality for the HPT, PUM and Z5 Lake Bed tuffs (Roberts et al., 2010; Hilbert-Wolf et al., 2017). B) Simplified stratigraphy of the Rukwa Rift Basin and volcanic episodes of the Rukwa–Malawi–Usangu Junction. Volcanic intervals sampled herein are shown in orange. PH = Panda Hill carbonatite, NFT = Nsungwe Formation Tuffs, TB = Tikuyu Basalt, UPh = Usangu phonolites, RVP = Rungwe Volcanic Province. Reported ages are from: (1) Mesko (2020); (2) Morisset (1993); (3) Roberts et al. (2012); (4) Rasskazov et al. (2003); (5) Ebinger et al. (1989); (6) Fontijn et al. (2012). (For interpretation of the references to colour in this figure legend, the reader is referred to the web version of this article.)

2. Geological setting

2.1. The East African Rift System

The EARS is an interconnected series of graben and half-graben basins hosted within a series of Precambrian continental orogenic belts and blocks that surround the Archean Tanzanian Craton (Fig. 1; Chorowicz, 2005; Begg et al., 2009). The EARS is divided into Eastern and Western Branches that run either side of the Tanzanian Craton. The Eastern Branch extends from the Afar triple junction in northern Ethiopia, through Kenya and into Northern Tanzania (Fig. 1). Rift development follows pre-existing weaknesses in the Pan-African Mozambique belt that formed during the collision between East and West Gondwana (ca. 650–580 Ma) (Chorowicz, 2005; Fritz et al., 2005; Ring, 2014). The Eastern Branch is characterised by voluminous, largely on-axis bimodal volcanism that follows a general north to south progression of rift development that initiated at ca. 40–30 Ma in northern Kenya (Morley et al., 1992b; MacDonald et al., 2001; Furman, 2007), at ca. 15 Ma and 12 Ma in central and southern Kenya, respectively (Morley et al., 1992b), and at 8 Ma in northern Tanzania (Dawson, 1992).

The Western Branch runs from western Uganda to southern Malawi and central Mozambique and is hosted in a complex series of basement terranes (i.e. the Rwenzori, Kibaran, Ubendian, and Irumide mobile belts) accreted along the western margins of the Tanzanian craton between ca. 2.1 Ga and 1 Ga (Fig. 1; Yoshida et al., 2003; Begg et al., 2009; Delvaux et al., 2012). Many of the rift basins in the Western Branch have undergone more than one period of activation, with Cenozoic rifting being associated with the reactivation of pre-existing Karoo-aged structures (Kilembe and Rosendahl, 1992; Morley et al., 1992a; Delvaux et al., 2012). Magmatism in the Western Branch is considerably less voluminous and occurs in a series of intra-basinal volcanic provinces initiating at ca. 25 Ma in the Rukwa–Malawi–Usangu junction (proximal to the Rungwe Volcanic Province) followed by both the Virunga Volcanic Province (ca. 12 Ma), Kivu Volcanic Province (ca. 8 Ma) and Toro Ankole Volcanic Field (ca. 50 ka) to the north (Fig. 1A; Ebinger, 1989; Ebinger et al., 1989; Kampunzu and Lubala, 2012; Roberts et al., 2012).

2.2. Local geology

The Rukwa–Malawi–Usangu junction is hosted within the Paleoproterozoic Ubendian belt between the Archean Tanzanian Craton to the NE, and the Paleoproterozoic Bangweulu Block (1.8 Ga) to the SW. The NW-SW trending Ubendian shear zone, developed via ~1.8 Ga deformation of ~2.1 Ga Usagaran Belt, governs basin development in the Cenozoic Rukwa Rift (Morley et al., 1992a; Delvaux et al., 2012). Basement rocks to the north of the Bangweulu Block beneath the Tanganyika Rift (and sections of the Western Branch further north) are associated with the Kibaran Orogeny (ca. 1.4 Ga; Ring, 2014). Crustal basement between the Bangweulu Block and Malawi Rift are associated with the ca. 1 Ga Irumide Orogeny (Hauzenberger et al., 2014; Ring, 2014). To the east of the Tanzanian Craton and the Malawi Rift is the Mozambique Belt (ca. 0.7 to 0.5 Ga), which also comprises the majority of the crustal basement to the Eastern Branch (Fig. 1B; Yoshida et al., 2003; Ring, 2014).

The Rukwa Rift has witnessed several periods of activation/reactivation, including episodes during the Permian (Karoo), Cretaceous, Paleogene and Neogene; each of which is preserved in the 8–10 km thick package of sedimentary infill (Kilembe and Rosendahl, 1992; Roberts et al., 2010; Mulaya et al., 2021). Alkaline magmatism has accompanied the three most recent episodes of activity and resulted in the Panda Hill and Mbalizi carbonatites (ca. 165–110 Ma; Morisset, 1993; Mesko, 2020; Sun et al., 2021) associated with deposition of the Cretaceous Galula Formation, the Nsungwe Formation Tuffs (herein NTF) associated with deposition of the Oligocene Nsungwe Formation (ca. 25 Ma; Roberts et al., 2012; Lawrence et al., 2021), and modern (ca. 9 Ma–recent) Rungwe Volcanic Province associated with deposition of the Lake Beds Group (Fig. 2; Ebinger et al., 1989; Ivanov et al., 1998; Fontijn et al., 2012; Hilbert-Wolf et al., 2017). Three stages of volcanic activity

are described for the Rungwe Volcanic Province; (1) Late Miocene: ca. 9.2–5.4 Ma; (2) Late Pliocene–Early Pleistocene: ca. 3–1.6 Ma, and; (3) Mid-Pleistocene–Recent: since ca. 0.6 Ma (Fig. 2). However, analysis of both primary and detrital igneous crystals from tuff beds of the Lake Beds Group suggests this activity may have been more continuous than currently recognised (Mtelela et al., 2016; Hilbert-Wolf et al., 2017; Mtelela et al., 2017).

Geophysical studies describe the local lithosphere beneath Rungwe–Malawi–Usangu junction and Rungwe Volcanic Province as being significantly thinned, which has been attributed elsewhere in the EARS to be a consequence of stagnation of the northward African plate motion between 30 and 19 Ma (Ebinger and Sleep, 1998; O'Connor et al., 1999; Njinju et al., 2019; Hopper et al., 2020). This coincides with an episode of thermal perturbation beneath the Rukwa–Malawi–Usangu junction, potentially resulting from long-lived flow stagnation and pooling of upwelling material against the cratonic root of the Tanzanian Craton (Grijalva et al., 2018; Tepp et al., 2018; Hopper et al., 2020). This feature is suggested to affect the flow direction and extent of magmatism in the Western Branch (Tepp et al., 2018).

An additional volcanic episode is recorded along the north-east boundary of the Rungwe Volcanic Province in the Usangu Basin during the early–mid Miocene (ca. 19–13 Ma) in the form of phonolitic cones and edifices (Rasskazov et al., 2003). However, no correlative rift-fill deposition or volcanic tephra is yet known in the Rukwa or Malawi Rifts during this time (Fig. 2; Kilembe and Rosendahl, 1992; Rasskazov et al., 2003; Roberts et al., 2010; Mesko, 2020). Previous studies of the 9 Ma–recent activity of the Rungwe Volcanic Province observed a strong relationship between the inherited NW-SE trending tectonic fabric of the underlying basement and the activation of normal faults and volcanism at the surface (Fontijn et al., 2010, 2012). Such tectonic controls were not observed for the older vents in the Usangu Basin. However, these outcrops, along with the NFT, clearly demonstrate an early period of lithospheric disturbance and Cenozoic magmatism prior to the development of the modern Rungwe Volcanic Province.

2.3. Sample description and rationale

Samples of the Panda Hill carbonatite (PH), NFT (AS18, TZ-1, BW-4, CM, WT) and Lake Beds Group tuffs (Pumice tuff [PUM], Hippo tuff [HPT], Pyro tuff [PY], and Z5 tuff, originating from the Rungwe Volcanic Province) were collected from known outcrops in the Rukwa Rift Basin (Fig. 2) during the 2014–2018 field seasons. Sample locations are provided in Supplementary Item A. Age data for the NFT are presented in Roberts et al. (2012), Stevens et al. (2013), and Spandler et al. (2016), with in-depth petrographic descriptions and mineral chemistry presented in Lawrence et al. (2021). Age data and descriptions for the Lake Beds Group tuffs are presented in Hilbert-Wolf et al. (2017) and Mtelela et al. (2017).

The NFT represent an isolated, early manifestation of phonolite-carbonatite volcanism and rift development in the Rukwa Rift at ca. 25 Ma (Roberts et al., 2012; Lawrence et al., 2021). The selected samples of Lake Beds tuffs represent weathered intermediate to felsic alkali volcanic deposits and cover the three recognised periods of increased volcanic activity in the Rungwe Volcanic Province at 8.7 Ma (PUM), 3.5 Ma (HPT) and < 1 Ma (PY and Z5). The Jurassic/Cretaceous Panda Hill and Mbalizi carbonatites represent earlier (ca. 165–116 Ma) period(s) of alkaline volcanism and basin development in the Rukwa Rift (Morisset, 1993; Mesko, 2020; Sun et al., 2021). Collectively, these samples provide a temporal framework for monitoring the lithospheric source of rift-associated magmatism in the Rukwa Rift over a time span exceeding 100 m.y.

Volcanic tuffs of the Rukwa Rift (particularly the NFT) are pervasively altered and dominated by devitrified clay matrixes, rendering them unsuitable for conventional whole-rock analysis. Furthermore, no vent or source is known for the NFT. Lawrence et al. (2021) utilised resistant igneous mineral separates and their inclusions to identify an igneous assemblage for the NFT that includes titanite, phlogopite, fluorapatite, clinopyroxene, Ti-rich andradite, sanidine, pyrochlore, nepheline, cancrinite, pyrrhotite, zircon, calcite, Na-REE-carbonate and phonolite silicate glass, which taken together characterizes represent the volcanic products of an early rift phonolite-carbonatite system (Lawrence et al., 2021). Of these, titanite, apatite, pyrochlore and zircon were shown to be significantly enriched in rare earth elements (REE) and are thus deemed excellent candidates for in-situ isotopic analysis (Lawrence et al., 2021).

In-situ isotopic analysis of individual crystals has the capacity to trace mineral-scale variations that cannot be monitored via whole-rock analysis (Hammerli et al., 2014; Spandler et al., 2018). For this reason, an in-situ approach was taken for all samples to generate a high resolution and internally comparable isotopic dataset spanning ca. 165 Ma to present. We evaluate the reliability of our in-situ results for Panda Hill and the Lake Beds Group tuff samples by comparison with previous whole-rock isotope analyses of Panda Hill and the Rungwe Volcanic Province, respectively. We also undertook bulk Sm-Nd and Rb-Sr isotope analyses of titanite crystal concentrates from two NFT samples and one Lake Beds Group tuff sample to further compare bulk and in-situ Sm-Nd isotope analysis results, and to extend the existing whole-rock Rb-Sr isotope data for magmatic rocks from the region.

3. Analytical procedures

3.1. Sample Preparation

Each of the samples was subject to heavy liquid and magnetic separation processes, as previously described in Lawrence et al. (2021), to produce heavy mineral concentrates. From these concentrates, pure mineral separates were hand picked, and then cleaned in milli-Q water in an ultrasonic bath for use in both bulk and in-situ isotope analysis. Primary igneous minerals selected for isotopic analysis include titanite, apatite, pyrochlore and zircon. These phases are enriched in the isotopes of interest and have been used to provide age control on the timing of volcanism (Roberts et al., 2012; Spandler et al., 2016; Hilbert-Wolf et al., 2017). Mineral grains for in-situ isotope analyses were set in 25 mm diameter epoxy resin mounts, polished to expose grain interiors, and then studied in detail using secondary electron imaging, backscattered electron imaging and cathodoluminescence imaging to inspect variability in mineral zonation.

3.2. Bulk titanite Sm-Nd and Rb-Sr isotope analysis

Bulk Sm-Nd and Rb-Sr isotope analysis of clean titanite separates was performed at the University of Adelaide with a Finnigan MAT262 thermal ionisation mass spectrometer (TIMS), in static and quadruple cup dynamic measurement modes following the routine described in Wade et al. (2006). Between 5 and 15 mg of the samples were digested in PARR acid (HNO_3-HF acid mix) digestion bombs at 190 °C for 96 h, then evaporated to dryness and bombed with 6 M HCl overnight. The samples were then spiked with a $^{150}Nd/^{147}Sm$ spike. The measurements were corrected for mass fractionation by normalisation to $^{146}Nd/^{144}Nd = 0.7219$. Neodymium and Sm concentrations were calculated by isotope dilution and were corrected for 100 pg and 50 pg blanks, respectively. Reference material JNdi-1 was 0.512107 ± 9 (2σ) and $^{143}Nd/^{144}Nd$ ratios were normalised to the TIMS value of the JNdi-1 glass (0.512098 ± 13; Fisher et al., 2011). Strontium isotope analyses follow the same digestion procedures as for Sm-Nd isotope analysis, followed by Sr separation carried out using 200 μL eichrom 50-100 μ Sr resin in Micro Bio-spin columns. The measurements underwent normalisation to $^{86}Sr/^{88}Sr = 0.1194$, using exponential mass fractionation correction. The $^{87}Sr/^{86}Sr$ ratios were normalised to the measured NIST SRM 987 TIMS value of 0.710238 ± 0.000011.

3.3. In-situ Sm-Nd isotope analysis

In-situ Sm-Nd isotope analysis of titanite, apatite and pyrochlore was undertaken at the Advanced Analytical Centre, James Cook University, Townsville, using a Coherent GeoLasPro 193 nm Excimer laser ablation system coupled with a Thermo-Scientific NEPTUNE multicollector ICP-MS. The NEPTUNE setup is the same as used by Hammerli et al. (2014) with interference and mass bias corrections made according to Fisher et al. (2011). Laser spot sizes of between 40 and 90 μm were used for titanite, apatite and pyrochlore depending on size and morphology of individual grains. Each analysis consisted of 60s on background and 60s data acquisition with a 60s washout time between analyses. Samples were ablated in a large volume cell using a repetition rate of 4 Hz and surface energy density (measured at the site of ablation) of 4 J/cm^2. The ablated material was carried via He gas (flow rate of 2.5 l/min) to a bulb with a volume of 2.5 cm^3 where it was mixed with Ar (flow of 0.95 l/min) and N_2 (0.01 l/min) before being carried to the MC-ICP-MS. A synthetic LREE-doped glass (ID-TIMS; $^{147}Sm/^{144}Nd = 0.2451 \pm 7$) and a Nd-doped glass (JNdi-1; ID-TIMS $^{143}Nd/^{144}Nd = 0.512098 \pm 13$) were used as primary standards to monitor and correct for drift in unknown $^{147}Sm/^{144}Nd$ and $^{143}Nd/^{144}Nd$ values (Fisher et al., 2011). Our results for JNdi-1 glass are $^{143}Nd/^{144}Nd = 0.512092 \pm 6$ ($n = 43$) and for LREE glass are $^{147}Sm/^{144}Nd = 0.2453 \pm 6$ ($n = 39$). As a quality control measure, Otter Lake apatite and MKED-1 titanite were used as secondary standards (see Supplementary Item B). Our results for Otter Lake apatite ($n = 17$; $^{143}Nd/^{144}Nd = 0.511915 \pm 24$ and $^{147}Sm/^{144}Nd = 0.0809 \pm 6$) align with the average values ($^{143}Nd/^{144}Nd = 0.511942 \pm 45$ and $^{147}Sm/^{144}Nd = 0.0827 \pm 21$) reported for Otter Lake (Yang et al., 2014). Our results for MKED-1 titanite ($n = 6$; $^{143}Nd/^{144}Nd = 0.511630 \pm 20$ and $^{147}Sm/^{144}Nd = 0.1268 \pm 14$) agree with those published by Spandler et al. (2016); $^{143}Nd/^{144}Nd = 0.511630 \pm 25$, and $^{147}Sm/^{144}Nd = 0.1270$. Some analyses returned errors >1 εNd unit due to low Nd concentrations or contamination of the analysis by inclusions. These analyses were excluded from the final dataset.

3.4. In-situ Lu-Hf isotope analysis

In situ Lu-Hf isotope analysis of zircon was conducted using the laser ablation and multicollector ICP-MS instrumentation as outlined above. The NEPTUNE set-up and isobaric interference corrections procedures follow that of Kemp et al. (2009). Each analysis consisted of 60 s on background and 60 s data acquisition with a 60 s washout time between analyses. Samples were ablated using a repetition rate of 4 Hz, a surface energy density of 6 J/cm^2, and a spot size of 65 μm. FC1 zircon was used as a secondary standard for quality assurance. We obtained average values of $^{176}Hf/^{177}Hf = 0.282483 \pm 8$ for Mud Tank and $^{176}Hf/^{177}Hf = 0.282175 \pm 9$ for FC1 zircon (Supplementary Item C). These values are within error of the solution value of FC1 of 0.282184 ± 16 (Woodhead and Hergt, 2005), and indistinguishable from the $^{176}Hf/^{177}Hf$ values determined by LA-MC-ICP-MS of 0.282499 ± 17 and 0.282176 ± 22 for Mud Tank and FC1, respectively (Kemp et al., 2009). As with the Sm-Nd isotope analyses, values with errors >1 εHf unit were deemed unreliable and excluded from the dataset.

4. Results

4.1. Sm-Nd and Rb-Sr isotopes of bulk titanite separates

Bulk Sm-Nd and Rb-Sr isotopes of titanite separates from four samples are presented in Table 1. The NFT samples AS18 and BW4 return similar measured $^{143}Nd/^{144}Nd$ values of 0.512727 and 0.512726 respectively, whereas NFT sample TZ-1 returned a $^{143}Nd/^{144}Nd$ value of 0.512647. This corresponds to εNd ($t = 25$ Ma) values of +2.05, +2.02 and + 0.49 respectively, which is in good agreement with the previous in-situ analysis of Spandler et al. (2016). Sample PY (<1 Ma) returned a $^{143}Nd/^{144}Nd$ value of 0.512456 and εNd of −3.54. NFT samples AS18, BW4 and TZ-1 return near indistinguishable measured $^{87}Sr/^{86}Sr$ ratios of 0.704171, 0.704175 and 0.704303 respectively, whereas PY returned a $^{87}Sr/^{86}Sr$ ratio of 0.706985. Given the low Rb contents of NFT (< 0.07 ppm) and PY (<0.4 ppm) titanites, the measured $^{87}Sr/^{86}Sr$ ratio is herein interpreted to represent the initial ratio.

4.2. In-situ Sm-Nd isotopes

Average isotopic analyses of igneous titanite, apatite and pyrochlore are presented in Table 2. Individual and standard analyses are presented in Supplementary Item D. Initial εNd values have been calculated using the 165 Ma age reported for Panda Hill (Mesko, 2020), 25 Ma age for the NFT (Roberts et al., 2012), 8.7 Ma and 3.5 Ma ages for PUM and HPT tuffs, respectively (Hilbert-Wolf et al., 2017), and 0.84 Ma for Z5 tuff (Roberts et al. pers. comm.).

Both Panda Hill apatite ($n = 7$) and pyrochlore ($n = 5$) return similar $\varepsilon Nd_{(i)}$ values ranging between 0 and + 1.5 (average = +0.76 ± 0.75; Fig. 3). Due to the similarity in Sm/Nd of Panda Hill pyrochlore and apatite, a meaningful isochron cannot be calculated from these two minerals. Analyses of NFT titanite from samples AS18 ($n = 15$), WT ($n = 10$) and BW4 ($n = 14$) show some variance in $\varepsilon Nd_{(i)}$ range between ~0 and + 2.4. Analyses of NFT sample TZ-1 ($n = 16$) titanite return two distinct $\varepsilon Nd_{(i)}$ populations, the first, in agreement with other NFT samples, of $\varepsilon Nd_{(i)}$ between +0.6 to +2.2 ($n = 9$) and the second returning lower $\varepsilon Nd_{(i)}$ values between −2.2 to −4.7 ($n = 8$) (Fig. 4). Younger samples from the Lake Beds sequence form tight groups around average $\varepsilon Nd_{(i)}$ values of −4.1, −3.4 and − 1.5 for the PUM (n = 9), HPT (n = 9) and Z5 (n = 7) samples respectively (Fig. 5).

4.3. In-situ Lu-Hf isotopes of zircon

Lutetium–Hf isotope analyses of Oligocene zircon from the NFT sample CM (Roberts et al., in-prep), and the Lake Beds samples PUM and HPT (Hilbert-Wolf et al., 2017) are presented in Table 3 and Supplementary Item E. These zircons are interpreted to be of volcanic origin (Hilbert-Wolf et al., 2017; Lawrence et al., 2021). Isotopic ratios of zircon from the NFT and HPT show greater variance with respect to measured $^{176}Lu/^{177}Hf$ and $^{176}Hf/^{177}Hf$, with values ranging from 0.000189 ± 2 to 0.003249 ± 52, and 0.282683 ± 13 and 0.282794 ± 26 respectively for the NFT, and between 0.001723 ± 9 to 0.004998 ± 62, and 0.282528 ± 10 to 0.282594 ± 15, respectively for the HPT. The $^{176}Lu/^{177}Hf$ and $^{176}Hf/^{177}Hf$ for the PUM sample are less variable with values between 0.002356 ± 4 and 0.005642 ± 11, and 0.282611 ± 14 and $282{,}650 \pm 20$, respectively. Calculated $\varepsilon Hf_{(i)}$ values for the NFT

Table 1
Bulk titanite Sm-Nd and Rb-Sr isotope data.

Sample	$^{87}Sr/^{86}Sr$	± 2σ	Nd ppm	Sm ppm	$^{147}Sm/^{144}Nd$	$^{143}Nd/^{144}Nd$	Age (Ma)	εNd (i)	Age DM (Ma)
AS18	0.704171	0.000004	1439	231	0.0972	0.512727	25	2.05	628
BW4	0.704175	0.000003	1434	233	0.0983	0.512726	25	2.02	630
TZ1	0.704303	0.000006	1471	237	0.0972	0.512647	25	0.49	746
PY	0.706985	0.000003	9194	1361	0.0895	0.512456	1	−3.54	1028

Notes: See Supplementary Item F for Depleted Mantle (DM) model age calculations. (i) = initial.

Table 2
Average in-situ Sm-Nd isotope values.

Sample	Mineral	$^{147}Sm/^{144}Nd$	± 2σ	$^{143}Nd/^{144}Nd$	± 2σ	Age (Ma)	$^{143}Nd/^{144}Nd(i)$	εNd(i)	± 2σ	Age DM (Ma)
Panda Hill										
PH	Pyrochlore	0.0851	0.0013	0.512563	0.000037	165	0.512471	0.89	0.72	870
PH	Apatite	0.0886	0.0013	0.512565	0.000036	165	0.512469	0.85	0.71	867
Nsungwe Formation Tuffs										
BW4	Titanite	0.1015	0.0003	0.512708	0.000028	25	0.512692	1.68	0.54	656
AS18	Titanite	0.0938	0.0004	0.512702	0.000028	25	0.512687	1.58	0.54	665
WT	Titanite	0.0952	0.0003	0.512640	0.000029	25	0.512624	0.35	0.57	757
TZ1*	Titanite	0.0926	0.0003	0.512693	0.000027	25	0.512678	1.41	0.54	678
Lake Beds Tuffs										
PUM	Titanite	0.0956	0.0015	0.512420	0.000015	8.7	0.512415	−4.14	0.29	1081
HPT	Titanite	0.0969	0.0022	0.512461	0.000032	3.5	0.512459	−3.40	0.32	1021
Z5	Titanite	0.0819	0.0028	0.512561	0.000014	1	0.512560	−1.49	0.36	873

Notes: * TZ1 average excludes outlier data (i.e. εNd below −2). See Supplementary Item F for Depleted Mantle (DM) model age calculations. (i) = initial.

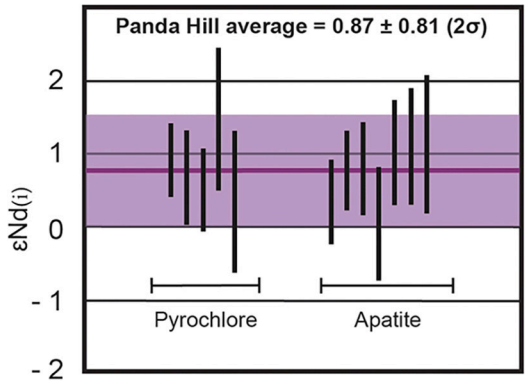

Fig. 3. Epsilon Nd values of individual analyses (vertical bars) of pyrochlore and apatite from Panda Hill. Length of the vertical bars represents 2σ error range. The purple horizontal line and shaded field represents the average value and 2σ error, respectively. (For interpretation of the references to colour in this figure legend, the reader is referred to the web version of this article.)

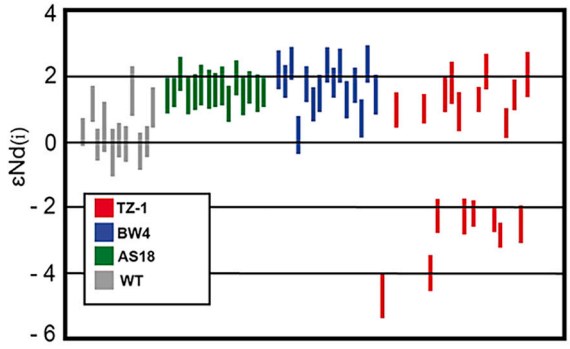

Fig. 4. Epsilon Nd values of in situ analyses of titanite for NFT. Length of vertical bars represents 2σ error range.

zircon (n = 5) are between +0.86 and − 1.41 with an average of −0.23 (±0.7) (Fig. 6). The Lake Beds samples PUM (n = 9) and HPT (n = 8) return respective average $\varepsilon Hf_{(i)}$ values of −5.5 (±0.6) and − 8.3 (±0.42) (Fig. 6).

4.4. Model enrichment age calculations

Given the silica-undersaturated alkaline nature of the magmatism in the Rukwa Rift (e.g., Lawrence et al., 2021), and the association of

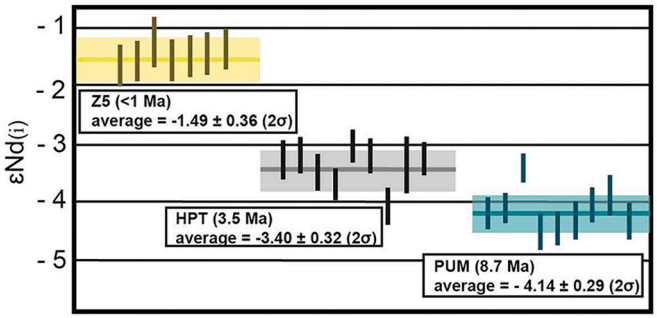

Fig. 5. Epsilon Nd values of in situ analyses of titanite from the Lake Beds tuffs. Length of vertical bars represents 2σ error range for each analysis. Yellow, grey and light blue horizontal lines and shaded fields correspond to sample average and 2σ error for the Z5, HPT and PUM tuffs, respectively.

alkaline magmatism with a mantle derivation (Yaxley et al., 2022), we assume that the volcanic rocks examined here were derived from an enriched mantle source that developed via ancient metasomatism of depleted mantle. To model the timing of mantle metasomatism, we therefore apply the two-stage Nd isotope model of Liew and Hofmann (1988) using the composition of enriched mantle xenoliths from across the southern EARS (Western Branch and southern Kenya) as representative of the enriched mantle source in the region. To complement these data, we also present depleted mantle model ages calculated based on our Lu-Hf isotope data for zircon (Table 3). Details of both model calculations and xenolith compositions are presented in Supplementary Item F.

Neodymium isotope mantle enrichment model ages for both the in-situ and bulk titanite from the NFT samples range from 628 to 757 Ma (Tables 1 and 2; average = 680 Ma): these compare well with the Hf isotope model ages for NFT sample CM of 637 to 785 Ma (average = 685 Ma; Table 3). Neodymium isotope mantle enrichment model ages for Panda Hill and the Lake Beds Tuff samples are ca. 870 Ma (PH), 1081 Ma (PUM), 1021 Ma (HPT), 1028 (PY) and 873 Ma (Z5). These also compare well with Lu-Hf isotope model ages for samples PUM (974 Ma) and HPT (1053 Ma) produced from in-situ zircon analyses.

5. Discussion

The radiogenic isotopic composition of alkaline and carbonatite rocks of the EARS, and elsewhere, are considered excellent probes of mantle source regions (Yaxley et al., 2022). This is largely attributed to a primary enrichment in trace elements, low magma temperatures and geologically rapid ascent rates associated with their parental magmas (e.

Table 3
In-situ Lu-Hf isotope values for zircon.

Sample		$^{176}Lu/^{177}Hf$	± 2σ	$^{176}Hf/^{177}Hf$	± 2σ	Age (Ma)	$^{176}Hf/^{177}Hf$ (i)	εHf (i)	± 2σ	Age DM (Ma)
Nsungwe Formation Tuff										
CM	Min	0.000189	0.000002	0.282731	0.000013	25	0.282729	−1.41	0.45	636
	Max	0.003249	0.000052	0.282794	0.000026	25	0.282794	0.86	0.92	785
	Average	0.001130	0.000016	0.282763	0.000020	25	0.282763	−0.23	0.70	696
Lake Bed Tuffs										
PUM	Min	0.002356	0.000004	0.282606	0.000014	8.7	0.282605	−6.17	0.50	914
	Max	0.005642	0.000159	0.282645	0.000020	8.7	0.282644	−4.80	0.71	1029
	Average	0.004152	0.000030	0.282627	0.000017	8.7	0.282626	−5.42	0.60	967
HPT										
	Min	0.001723	0.000009	0.282522	0.000010	3.5	0.282522	−9.22	0.35	957
	Max	0.004998	0.000062	0.282589	0.000015	3.5	0.282588	−6.87	0.52	1151
	Average	0.002982	0.000032	0.282548	0.000012	3.5	0.282548	−8.32	0.42	1053

Notes: See Supplementary Item F for Depleted Mantle (DM) Model age calculations.

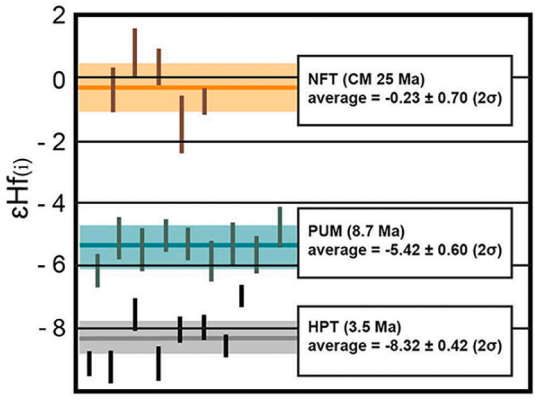

Fig. 6. Epsilon Hf values of individual zircon analyses for NFT (sample CM; orange), PUM (light-blue), HPT (grey) Lake Beds Tuffs. Length of coloured vertical bars represents 2σ error range for each analysis. Orange, light-blue and grey horizontal lines and shaded fields correspond to sample average and 2σ error for the CM, PUM and HPT tuffs, respectively. (For interpretation of the references to colour in this figure legend, the reader is referred to the web version of this article.)

g., Walter et al., 2021), all which can provide resistance against chemical and isotopic contamination of crustal component during magma transit towards the surface (Bell and Tilton, 2001). The NFT have a characteristic mineral assemblage that is consistent with a phonolite-carbonatite source (Lawrence et al., 2021). Within this assemblage, trace-element rich mineral phases (such as titanite, apatite and pyrochlore used in this study) offer an opportunity to investigate the magmatic source of the extensively weathered NFT and Lake Beds tuffs. The Panda Hill and Mbalizi carbonatites, and alkaline lavas of the Rungwe Volcanic Province have been shown previously (via whole-rock analysis) to reflect the isotopic character of their mantle source (Furman, 1995; Bell and Tilton, 2001; Castillo et al., 2014; Sun et al., 2021). Therefore, the single crystal in-situ methods adopted for the Panda Hill and the Lake Beds tuff mineral separates presented in this study can be used to test the compatibility between conventional whole rock and in-situ isotope analysis approaches and, by extension, the accuracy and reliability of our in-situ results.

Bell and Tilton (2001) provide $^{143}Nd/^{144}Nd$ and $^{87}Sr/^{86}Sr$ data for the Panda Hill carbonatite (including the data of Morisset (1993)) where initial εNd values are between 0 and + 0.6 (t = 116 Ma, Morisset (1993)). Recalculated using the new age for Panda Hill of 165 Ma as reported by Mesko (2020) increases the εNd values to between +1.2 to +1.8. Although $^{87}Sr/^{86}Sr$ analyses were not conducted for Panda Hill in our work, we defer to the $^{87}Sr/^{86}Sr$ values presented by Bell and Tilton (2001) (who consider these initial ratios due to exceedingly low Rb) of between 0.7037 and 0.7042 (Fig. 7) as representative. Sun et al. (2021) reported initial εNd of +0.9 and $^{87}Sr/^{86}Sr$ of 0.704198 for the ca. 116 Ma Mbalizi carbonatite, located 15 kms NW of Panda Hill. For the Cenozoic lavas of the Rungwe Volcanic Province, Furman and Graham (1994) report εNd values between −0.4 and − 4.5, and $^{87}Sr/^{86}Sr$ of between 0.7046 and 0.7055. These values have since been corroborated by Castillo et al. (2014) who report $^{143}Nd/^{144}Nd$ values between 0.512619 and 0.512417 (εNd between −0.16 and − 4.1; t = 0 calculated here) and slightly extend the $^{87}Sr/^{86}Sr$ range of Rungwe lavas to between 0.704603 and 0.706920 (Fig. 7).

Our measured in-situ data of Panda Hill apatite and pyrochlore ($^{143}Nd/^{144}Nd$ = 0.512527 to 0.512594; $\varepsilon Nd_{(i)}$ = +0.4 to +1.6; Fig. 3) conform well with previous whole-rock analyses (Fig. 8). Similarly, the reported sample averages and individual Sm-Nd isotope spot analyses of titanite ($^{143}Nd/^{144}Nd$ = 0.512401 to 0.512573; εNd = −4.3 to −0.7; Fig. 5) from the Lake Beds tuff samples are in agreement with ranges previously defined by Castillo et al. (2014) for whole-rock analysis of uncontaminated lavas of the Rungwe Volcanic Province (Fig. 8). This is also the case for our bulk titanite Sm–Nd–Sr isotope results of Lake Beds tuff sample PY ($^{143}Nd/^{144}Nd$ = 0.512456; εNd = −3.55 and $^{87}Sr/^{86}Sr$ = 0.706985; Figs. 7 & 8), which returned values similar to the most isotopically enriched TAZ09–12 ($^{143}Nd/^{144}Nd$ = 0.512417 and

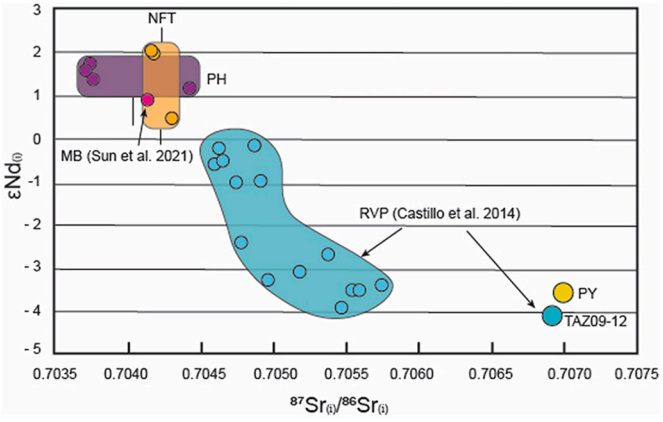

Fig. 7. $^{87}Sr/^{86}Sr$ vs initial εNd diagram for Panda Hill (PH – purple, This study), Mbalizi carbonatite (MB – pink; Sun et al., 2021) NFT (orange, This study) and the Rungwe Volcanic Province (RVP – blue, Castillo et al., 2014; PY – yellow, this study). Circle symbols correspond to whole rock data points, and fields represent hypothetical isotopic space based on the variation in whole-rock data. Note, the whiskers on PH and NFT fields represent total variations in εNd returned via in-situ analysis. Samples PY and TAZ09–12 of Castillo et al. (2014) are the most isotopically enriched analyses of the RVP. (For interpretation of the references to colour in this figure legend, the reader is referred to the web version of this article.)

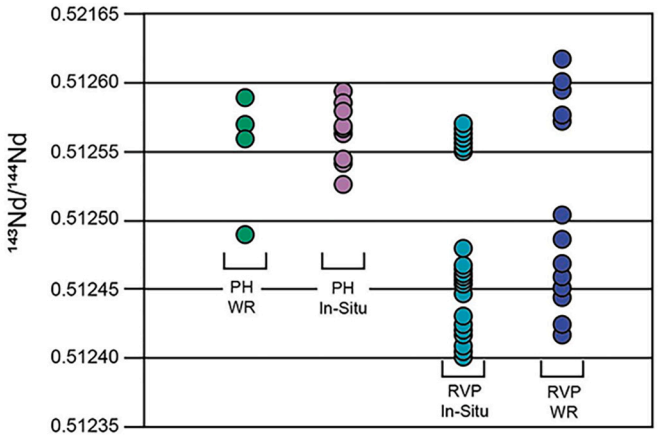

Fig. 8. Comparison between whole rock (WR) and in-situ Sm-Nd isotopes for Panda Hill (PH; Bell and Tilton, 2001) and Rungwe Volcanic Province (RVP; Castillo et al., 2014). Note the general consistency in ranges and values returned for both the PH and RVP, irrespective of method.

$^{87}Sr/^{86}Sr = 0.706920$) sample presented by Castillo et al. (2014). The average εHf of −5.42 and − 8.32 for the 8.7 Ma and 3.5 Ma Lake Beds tuff samples, respectively, fall within range of those reported from whole-rock analysis of uncontaminated lavas elsewhere in the Western Branch (εHf = −8.8 to −0.1; Rosenthal et al., 2009).

Together, the high degree of compatibility between our in-situ data and the published bulk-rock data demonstrate the capacity for in-situ analyses of single minerals to accurately reflect the magma source region in this locality, with a specific advantage that the in-situ approach can avoid complications of post-magmatic alteration and/or weathering, as is the case for the NFT.

5.1. Isotopic constraints of the NFT

The resolution provided by our in-situ Sm-Nd isotope data capably resolves the observed discrepancy between bulk Sm–Nd–Sr isotope data of sample TZ-1 (εNd = +0.49) and those of BW4 and AS18 (εNd = +2.02 and + 2.05, respectively). Whereas in-situ data of AS18 and BW4 agrees with bulk analyses, in-situ analyses of TZ-1 reveals the presence of two clearly distinct populations (εNd = +0.6 to +2.2; and εNd = −2 to −4.7; Fig. 4). Our results for sample TZ-1 provides a resolution not attainable using bulk analyses whereby more than one population is present in a sample. Specifically, that multiple single crystal analyses from a sample can reliably detects populations of grains, whereas bulk analysis may return a mixed isotopic result. Notwithstanding, bulk analysis of NFT samples form a restricted array around values of εNd +2 to 0, which is consistent with previous Sm-Nd isotope results for the NFT from Spandler et al. (2016). Although a slight variation observed within the representative in-situ Sm-Nd data of the NFT may reflect two overlapping yet discrete populations (i.e. at εNd +1.5 and + 0.5 respectively; Figs. 4 & 8), they remain well within values previously reported for East African carbonatites, including the nearby Panda Hill and Mbalizi (Bell and Tilton, 2001; Rooney, 2020 and references therein; Fig. 7) and are thus considered representative of their magmatic source.

The less radiogenic TZ-1 population (εNd = −2 to −4.7) uncovered from the in-situ titanite analyses is notably different to both bulk and in-situ NFT analyses in this study and elsewhere (Spandler et al., 2016; Lawrence, 2021). There is little evidence from the data for gradual mixing (i.e. progressive range between endmembers), rather two distinct populations are present. Assimilation of Proterozoic crustal basement or primary generation from a more isotopically-enriched lithospheric source are competing possibilities that may be considered in order to account for the observed variations.

The Ubendian Proterozoic crustal basement traversed by NFT magmas en-route to the surface is significantly enriched ($\varepsilon Nd_{(25\ Ma)} > -21$; Manya, 2011). Lawrence (2021) utilised the Sm-Nd isotopic values of NFT titanite and SiO_2 content of phonolitic melt inclusions in titanite to model potential crustal assimilation via an open system magma evolution scenario. In this case, no variation in εNd with increasing melt SiO_2 content was observed, indicating crustal assimilation was insignificant in this case. We also find no evidence for a shift in chemical compositions from peralkaline magmas towards peraluminous compositions, as would be expected with significant melting and assimilation of intermediate to felsic crust (Gao et al., 2016). Moreover, alkaline magmas (and in this case igneous crystals from these magmas) tend to be highly enriched in incompatible elements such as REE, Zr, Hf, Th and U compared to crustal rocks, which provides significant buffering capacity against isotopic modification via crustal contamination. Further evidence against crustal contamination includes the low magmatic temperatures of the NFT magmas (Lawrence et al., 2021) and lack of trace element indicators of crustal assimilation (e.g., negative Eu or Nb-Ta anomalies) in the NFT minerals and melt inclusions (Lawrence, 2021; Lawrence et al., 2021). Of note, the more radiogenic TZ-1 population is within the total range of uncontaminated lavas of the Rungwe Volcanic Province, so an alternative consideration is that these data may reflect the contribution of an additional mantle (rather than crustal) component (Furman, 1995; Castillo et al., 2014; Mesko, 2020). Nonetheless, with our current dataset we are unable to investigate the origin of this isotopic signature further. Instead, we henceforth focus on the bulk of the NFT data across all samples, as well as from Spandler et al. (2016), that returned coherent εNd values of +1.5 ± 1.

There are few Hf isotope data for EARS volcanic rocks compared with other radiogenic isotope systems such as Sm-Nd or Rb-Sr. Moreover, analyses of zircons from alkaline igneous rocks often return a range of εHf values indicative of isotopic disequilibria or a complex crystallisation history for zircon from these rocks (e.g., Sun et al., 2021, and refs. therein). Our in-situ Hf isotope analyses of NFT zircon (average εHf = −0.23), is based on limited analytical data, but in general is consistent with the Nd isotope results for these rocks (Fig. 4). Likewise, our εHf values for the Lake Beds Group tuffs of −5.42 and 8.32 (Fig. 6) are consistent with the relatively unradiogenic Nd isotope signature of these samples (Fig. 5).

5.2. Isotopic evolution through time

The Sm–Nd–Sr isotopic data of the NFT overlap with values previously reported for the Panda Hill and Mbalizi carbonatites, and are less enriched with respect to both Nd and Sr isotopes than values reported for the uncontaminated lavas of the Rungwe Volcanic Province (Figs. 7 & 9). These data suggest that the lithospheric source region responsible for local alkaline magmatism from ca. 165 Ma – 25 Ma may be isotopically distinct from that of late Miocene – recent magmatism in the Rungwe Volcanic Province for which there is no known carbonatite association. Temporally, the in-situ Sm-Nd isotope data of Panda Hill, NFT, and Lake Beds Group tuff samples (and the bulk Sm–Nd–Sr isotope data of Castillo et al. (2014), Bell and Tilton (2001) and Sun et al. (2021) for the modern Rungwe lavas, Panda Hill, and Mbalizi, respectively) are consistent with the contribution of a more isotopically enriched lithospheric source in modern Rungwe lavas. In this sense, the isotopic signature of magmatic products locally from 25 Ma, becomes increasingly enriched, with decreasing εNd and increasing $^{87}Sr/^{86}Sr$ through time (Figs. 7 & 9). Consistent with Sr-Nd isotope data, an enrichment through time is also reflected in the Lu-Hf isotopic system with εHf = −0.23 (25 Ma), εHf = −5.42 (8.7 Ma) and εHf = −8.32 (3.5 Ma) for the NFT and Lake Beds tuffs, respectively (Table 3).

5.3. Isotopic characteristics and possible lithospheric sources for the NFT

In synthesising the isotopic data collected from Cenozoic rift lavas of the EARS over the past few decades, Rooney (2020) grouped proposed

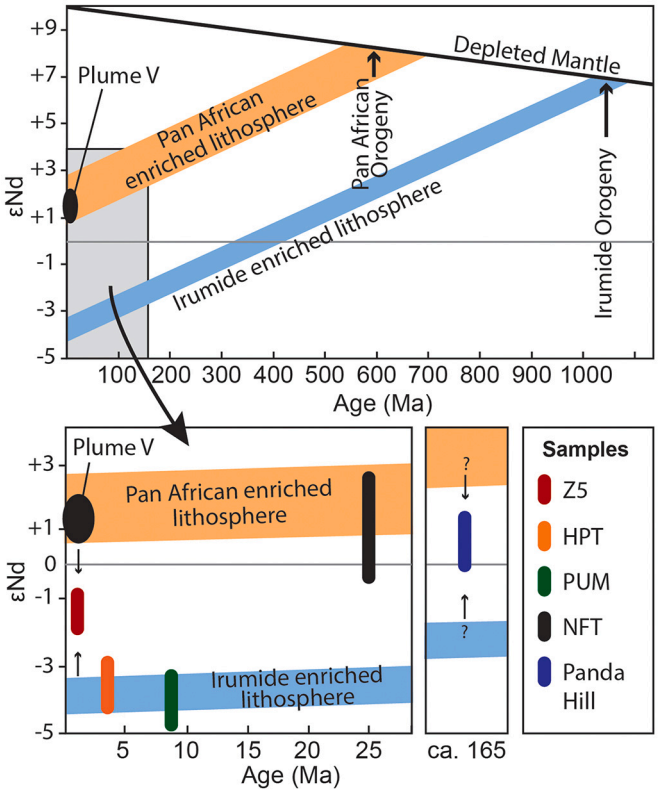

Fig. 9. Epsilon Nd versus time of calculated enriched mantle lithosphere reservoirs and alkaline magmas of the Rukwa Rift and Rungwe Volcanic Province. Enriched mantle arrays were calculated using the average Sm/Nd of enriched mantle xenoliths from the southern EARS projected back to the depleted mantle curve at the Pan-African and Irumide Orogenys. See the text and Supplementary Item F for details. The Plume-V compositions is from Castillo et al., 2014. Note that NFT samples and the 3.5 Ma and 8.7 Ma Lake Beds tuff samples are consistent with derivation from a Pan-African lithospheric source, and Irumide lithospheric source, respectively.

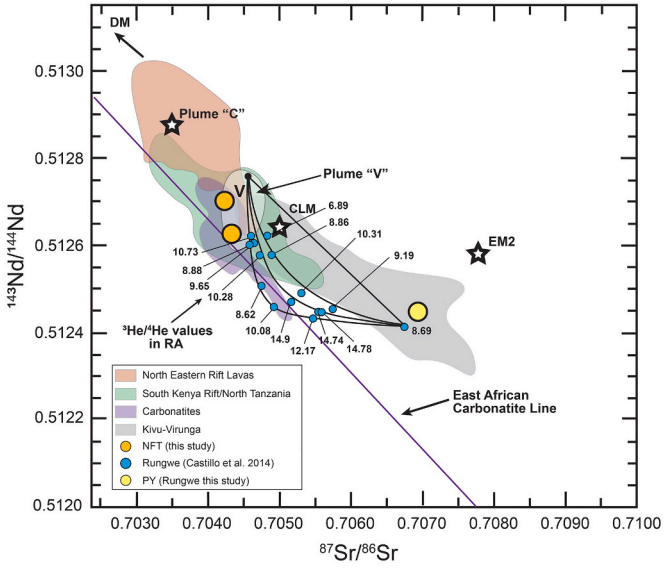

Fig. 10. $^{87}Sr/^{86}Sr$–$^{143}Nd/^{144}Nd$ data of mafic Quaternary rocks of East Africa adapted from Rooney (2020) with the addition of bulk isotopic data of NFT and PY (this study) and the individual points for whole rock isotopic data of Castillo et al. (2014). Depleted Mantle (DM) and Afar Plume "C" endmembers are from Rooney et al. (2012), Plume "V" and $^{3}He/^{4}He$ ratios are from Castillo et al. (2014), CLM component is from Furman and Graham (1999), and the East African Carbonatite line is from Bell and Tilton (2001). Note, the Plume-V component and proposed mixing curves (from Castillo et al. (2014) for Rungwe samples are inconsistent with the reported $^{3}He/^{4}He$ ratios for each respective sample (shown in R_A). NFT (significantly older than data fields shown for Quaternary rocks) isotopic reservoir is consistent with other East African carbonatites and youngest rocks of the South Kenya/North Tanzania rift lavas emplaced on cratonic lithosphere subjected to the Pan-African Orogeny. The isotopic evolution and variation observed in modern Rungwe lavas more closely resembles that of Kivu-Virunga western rift volcanic provinces whereby more complex and ancient lithospheric mantle components proposedly exist.

models for rift magmatism into those that emphasise: the presence of a plume, the absence of a plume (i.e. predominantly lithospheric), or a hybrid (influence of both plume and lithosphere components). Within these models, potential isotopic reservoirs (source regions) of rift lavas include the convecting (depleted) upper mantle, enriched metasomatic assemblages (i.e. amphibole-, phlogopite- and carbonate-bearing metasomes within the continental mantle lithosphere), and Plume-"C" (linked to the African LLSVP, high $^{3}He/^{4}He$ ratios and otherwise isotopically typified in the Afar; Fig. 10; Rooney, 2020).

The similarity between in-situ and bulk-rock Sm–Nd–Sr isotope analyses of Panda Hill and the NFT indicates they may share a common lithospheric source and/or process of formation. Unlike the majority of available Rungwe data, the NFT (and Panda Hill/Mbalizi) data reside within a field previously defined by Castillo et al. (2014) as "Plume-V" (Fig. 10). The proposed Plume-V source is isotopically constrained via the Nd–Sr–Pb isotopic signatures of the Nyiragongo volcano of the Virunga Volcanic Province (Chakrabarti et al., 2009) and via elevated $^{3}He/^{4}He$ ratios (>9 R_A) measured throughout the EARS (Castillo et al., 2014; Fig. 10). Importantly, while the presence of high $^{3}He/^{4}He$ ratios in young Rungwe lavas and throughout the Eastern Branch to the Afar substantiates the presence and contribution of a deeply-sourced mantle plume, the $^{3}He/^{4}He$ ratios and modelled isotopic mixing between Plume-V and lithospheric reservoirs (as suggested by Castillo et al. (2014)) are inconsistent with the Sr-Nd isotope data. As shown in Fig. 10 and discussed by Rooney (2020), the Sr-Nd isotope data of Castillo et al. (2014) sees the highest $^{3}He/^{4}He$ ratios (proposed greatest plume influence) plot further away from the proposed Plume-V endmember in Sr-Nd isotopic space. Rooney (2020) also notes discrepancies in the $^{3}He/^{4}He$ with respect to the Pb isotopic data presented of the proposed Plume-V. Thus, the enrichment we observe in local magmatism from 25 Ma to 8.7 Ma (i.e., a reduction in $^{143}Nd/^{144}Nd$ and increase in $^{87}Sr/^{86}Sr$ ratios, as well as decrease in εHf in our data), and the mixture of isotopic ratios for the Rungwe Volcanic Province (as presented by Castillo et al., 2014), is independent of the deep 'Plume' source that is likely responsible for elevated $^{3}He/^{4}He$ ratios measured at this locality.

An alternative offered by Rooney (2020) is that the Sr-Nd isotopic composition of the plume reservoir responsible for high $^{3}He/^{4}He$ throughout the EARS reflects that of the Afar Plume (Plume "C"; Fig. 10) and the region termed Plume-V (where the NFT reside, Fig. 10) more likely represents the 'common lithospheric mantle'. As described by Furman and Graham (1999) and Rooney et al. (2014), this reservoir formed as a result of regional metasomatic events impacting the base of the lithosphere surrounding the Tanzanian Craton between 1000 and 500 Ma. In such a model, the trace element and isotopic expression of rift lavas is intimately linked to the presence of volatile-rich assemblages in the mantle source (i.e. carbonate-, amphibole- and/or phlogopite-bearing mantle metasomes). Herein, isotopic variance observed within (and between) volcanic regions of the EARS is interpreted to reflect localised lithospheric heterogeneity. The heterogeneity itself reflects the metasomatic (orogenic) and/or melting histories of individual volcanic provinces.

Subduction-related metasomatism of the ancient convergent-margin orogens surrounding the Tanzanian Craton represent a mechanism to create local, isotopically-enriched assemblages in the lithosphere. As highlighted by previous studies, successive orogenic events may have produced multiple distinct metasomatic reservoirs that persist in the

continental lithosphere of the Western Branch (Furman, 1995; Rogers et al., 1998; Furman and Graham, 1999; Hudgins et al., 2015). Modelling based on isotopic studies of volcanic rocks from the EARS and continental rifts elsewhere (e.g. the Labrador Sea) conceptualise a layered lithosphere (Furman, 1995; Rogers et al., 1998; Furman and Graham, 1999; Tappe et al., 2007) where the youngest and least isotopically-evolved reservoir exists at the base and is the first to contribute melt at the onset of rift development. When thermo-mechanically perturbed, volatile-rich assemblages produce low viscosity melts that contribute disproportionally to early magma genesis. Consequently, the remnant denser metasomatic assemblages are gravitationally unstable and prone to foundering in the surrounding mantle asthenosphere (Furman et al., 2016). With continued melting, destabilisation and lithospheric thinning, more ancient and isotopically-enriched portions of the mantle lithosphere become exposed to melting (and/or thermal perturbation) and contribute to the isotopic character of lavas erupting at the surface.

If we consider this model of a layered lithosphere, the earliest-formed (i.e., oldest) local magmas will incorporate the most recently-formed metasomatic assemblages (i.e. youngest lithospheric reservoirs) with the contribution of more ancient and isotopically evolved regions being expressed in the younger lavas. Depleted mantle (DM) enrichment ages of 630 to 780 Ma from both Sm-Nd and Lu-Hf isotope data (Tables 1-3), for the NFT magmas appear to be products of melting of a lithospheric source that was enriched during the Pan-African Orogeny (550–700 Ma; Ring, 2014; Fig. 9). A similar Pan-African mantle enrichment event is proposed as the source of alkaline lava from the Ethiopian Plateau (Rooney et al., 2014). The Cretaceous Panda Hill and Mbalizi carbonatites may be melt products of highly enriched Pan African lithosphere, or mixed lithospheric/asthenospheric sources (Fig. 9). The respective Sm-Nd and Lu-Hf isotope mantle enrichment ages calculated for the older Lake Beds Group tuff samples (ca. 920 Ma to ca. 1150 Ma) reflect a period of lithospheric enrichment that broadly coincides with the Irumide Orogeny at 1.1 to 1.0 Ga (Ring, 2014). Collectively, these data are generally consistent with melting of a layered lithosphere, with local removal of the Pan-African-aged enriched base occurring between 25 Ma and 8.7 Ma.

The hypothesis that the enriched signatures observed for the Rungwe Volcanic Province are indeed that of exposure and melting of more ancient lithospheric assemblages, necessitates that the local lithosphere beneath the Rungwe has experienced a degree of thinning. Recent geophysical studies focused on the northern Malawi Rift extending to the Rungwe Volcanic Province reveal a mantle lithosphere that is indeed anomalously thinned and suggest that this occurred prior (or during) the very early stages of EARS development (Borrego et al., 2018; Grijalva et al., 2018; Tepp et al., 2018; Njinju et al., 2019; Hopper et al., 2020). The discovery of the NFT in the Oligocene sedimentary archive of the early Rukwa Rift are also supportive of early lithospheric perturbation and rift development (Hopper et al., 2020). The radiogenic isotope data presented here provide useful temporal constraints as to when such an event may have occurred, which appears to be coeval with rift development in the Eastern Branch (~30 to 25 Ma; Roberts et al., 2012). On this basis, a conceptual model for geological history for the Rukwa Rift is presented for future consideration (Fig. 11).

5.4. *Model of the geological evolution of the Rukwa Rift Basin and Rungwe Volcanic Province*

The Late Jurassic to recent volcanic and sedimentary history of the Rukwa Rift Basin can be summarised into four stages: (1) depositional regime accompanied by carbonatite volcanism at Panda Hill and Mbalizi during the Late Jurassic-Cretaceous (Morisset, 1993; Roberts et al., 2010; Mesko, 2020; Sun et al., 2021); (2) an early punctuated episode of deposition accompanied by the alkaline-carbonatite volcanism of the

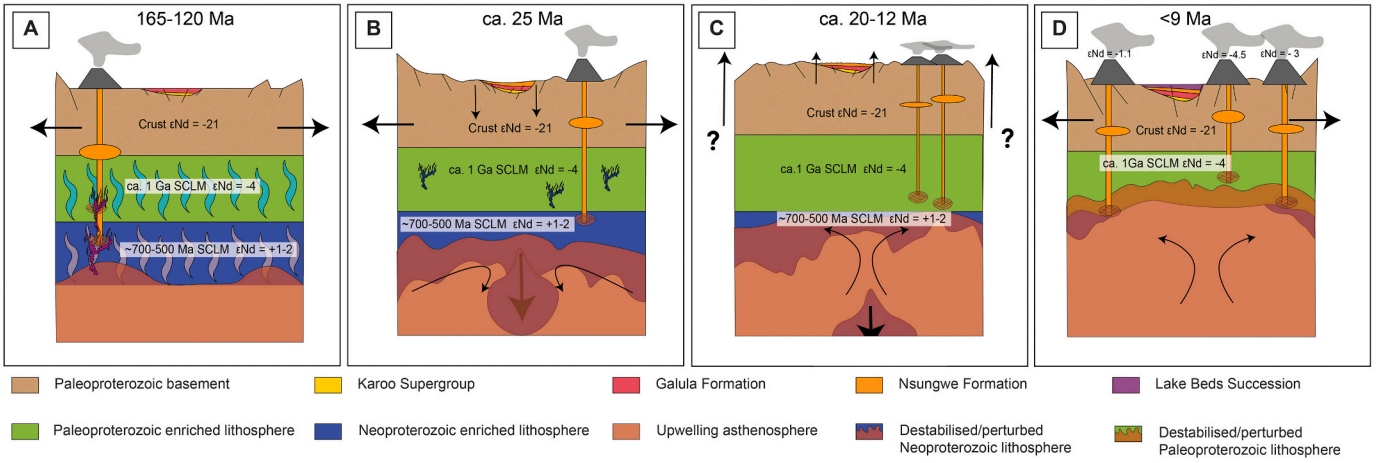

Fig. 11. Geological evolution of the Rukwa Rift and Rungwe Volcanic Province. A) Stage 1: Late Jurassic to Cretaceous: Crustal extension, basin subsidence and deposition accompanied by decompression melting produces carbonatite volcanism at Panda Hill and Mbalizi from either ultra-enriched Pan-African-aged metasomatised lithosphere (not modelled here), or mixed lithospheric mantle sources. B) Stage 2: Late Oligocene: Slowing of the African plate over the LLSVP causes chemical and mechanical destabilisation (shown here as a drip) of the Pan-African metasomatised lithospheric mantle beneath the Rukwa–Malawi–Usangu junction. This produces an early punctuated episode of basin subsidence and deposition of the Nsungwe Formation accompanied by phonolite–carbonatite volcanism of NFT. Lithospheric foundering (sagging of the crust) sees the structural reactivation of the Rukwa Rift and a shift in paleo-drainage pattern towards and inwardly draining basin (Roberts et al., 2010, 2012). The thermo-chemical destabilisation of lithospheric mantle produced the accompanying carbonatite magmatism of NFT; the isotopic signatures reflects production from dominantly Pan-African metasomatised mantle lithosphere (metasomes). C) Stage 3: Early-mid Miocene: Isostatic rebound of the crust after lithospheric detachment. Continual melting of remnant Pan-African and newly exposed Irumide lithosphere produces magmatism. Devolatilisation of sinking drip and melt interaction produces hybridised Pan-African/Irumide isotopic reservoirs (metasomes) in the heterogenous continental lithosphere. No basin subsidence or deposition is known during this time; instead the Red Sandstone Group likely underwent denudation/erosion due to regional uplift. D) Stage 4: Late Miocene to present: Continued heating of exposed ancient mantle lithosphere throughout the Miocene facilitates extension, thermal uplift of rift flanks and basin formation accompanied by more voluminous bimodal alkali magmatism in the RVP. The isotopic character of RVP magmatism reflects the incorporation and mixing between newly-exposed Irumide-aged enriched lithosphere (and/or metasomes) and hybridised lithosphere (and/or metasomes) produced via prior melting of Pan-African lithosphere. (For interpretation of the references to colour in this figure legend, the reader is referred to the web version of this article.)

NFT in the late-Oligocene (ca. 25 Ma) (Roberts et al., 2010, 2012); (3) a period of Miocene (19–14 Ma) volcanism in the Usangu Basin and Rungwe Volcanic Province during which there is no known basin subsidence or deposition; instead the sedimentary archive records an erosional discontinuity (Rasskazov et al., 2003; Roberts et al., 2010; Mtelela et al., 2017; Mesko, 2020) and; (4) late-Miocene (ca. 9 Ma) to recent extension and deposition accompanied by more voluminous bimodal magmatism in the Rungwe Volcanic Province (Fontijn et al., 2012; Hilbert-Wolf et al., 2017; Mtelela et al., 2017). In addition, sedimentary provenance and paleo-drainage analysis of the Rukwa Rift Basin records a shift from NW-SE sediment supply and drainage regime to an inwardly draining basin at the onset of stage 2 (Roberts et al., 2010, 2012). Geophysical (Hopper et al., 2020) and isotopic investigations (this study) indicate the mantle lithosphere experienced thinning in the time between stage 2 and 3 (25 to 9 Ma) during which the Rukwa Rift Basin experienced uplift, tilting, and erosion of the Nsungwe Formation (evidenced by a significant basal conglomerate at the base of the Lake Beds Group) prior to the modern extension regime of stage 4 (Roberts et al., 2012; Mtelela et al., 2017).

A significant reduction in the northward motion of the African plate between 30 and 25 Ma resulted in a stagnation of Eastern Africa over the African LLSVP and the initiation phases of rift development in both the Eastern and Western Branches of the EARS (O'Connor et al., 1999; Roberts et al., 2012; Rooney, 2017). In the Rukwa Rift, stagnation of the African plate over the LLSVP contributed to the pooling of upwelling material against the southernmost root of the Tanzanian Craton and the destabilisation of the lower lithospheric mantle beneath the Rungwe Volcanic Province (Tepp et al., 2018; Hopper et al., 2020). Physical destabilisation resulted in the structural reactivation and sagging of the Rukwa Rift Basin, as evidenced by a shift in paleo-drainage (draining inwardly) and the development of a lacustrine depositional regime at ca. 25 Ma (Roberts et al., 2010, 2012). The thermo-chemical destabilisation of the lower lithospheric mantle produced the accompanying phonolitic–carbonatite magmatism of the NFT, the isotopic signatures of which reflects production from Pan-African aged metasomatised mantle lithosphere.

The above geological observations and subsequent period of basin inversion and erosion (ca. 25–9 Ma) recorded in the stratigraphy of the Rukwa Rift Basin, and persistent magmatism during the Miocene in and around the Rungwe Volcanic Province (Rasskazov et al., 2003; Mesko, 2020) is consistent with isostatic rebound and continued melt contribution to surface volcanism following detachment of a foundering lithosphere (or lithosphere drip; shown in Fig. 11; Furman et al., 2016). The precise timing of lithospheric foundering is very difficult to quantify, but in this case we can broadly constrain the timing to between 25 and 9 Ma, based on the sedimentary record of inversion at Rukwa. Heating of exposed ancient mantle lithosphere throughout the Miocene facilitated the extensional regime in the present day Rukwa Rift Basin. As shown here, the isotopic character of accompanying voluminous magmatism in the Rungwe Volcanic Province reflects the incorporation and potential mixing between newly-exposed Irumide-aged enriched lithosphere and that responsible for the NFT (i.e. peripherally exposed or sinking Pan-African mantle). As suggested by Furman et al. (2016), the occurrence of lithospheric detachments may be important in the evolution of magmatism elsewhere in the EARS, but particularly in the Western Branch where volcanism is most prevalent in isolated interbasinal volcanic provinces superimposed on ancient and complex lithospheric terrains. Identifying lithospheric drip magmatism remains challenging and contentious (e.g., Rooney, 2020). We highlight that our approach of integrating the temporal evolution of volcanism recorded in isotope geochemistry with the sedimentological record of crustal response to lithosphere foundering can provide a compelling geodynamic case to support such a process.

6. Conclusions

The lithospheric foundations of the Western Branch record a complex and long-lived metasomatic history that has a profound influence on the composition of the western rift lavas. Evidently, the timing and nature of processes governing continent formation exert a strong influence on these same parameters during continental-scale tectonic stress and ultimately break-up. Single crystals from weathered volcanogenic strata of the Rukwa Rift Basin capably record and preserve the character and evolution of the lithospheric mantle in the Rungwe–Malawi–Usangu region. With these data we conclude that:

- The earliest manifestation of magmatism associated with the development of the Western Branch at 25 Ma (NFT) appear to be generated from a long-lived and common lithospheric component that may have persisted beneath the Rungwe–Malawi–Usangu locality since the Mid-Mesozoic. These compositions are also observed in the carbonatite and uncontaminated Quaternary lavas of Southern Kenya and Northern Tanzania, proximal to the Tanzanian Craton and Pan-African aged Mozambique Belt suture zone.
- The isotopic variability observed in lavas from the mid Miocene-Recent Rungwe Volcanic Province (combined with geophysical and sedimentological data), support a hypothesis of a layered lithosphere that experienced thinning (via lithospheric foundering) at the end of the Oligocene for the Rungwe–Malawi–Usangu region. In such a scenario, the presence and mixing between eroded Pan-African- and recently exposed Irumide-aged enriched lithosphere is the primary influence on the isotopic fingerprint of Rungwe lavas.

Declaration of Competing Interest

The authors declare that they have no known competing financial interests or personal relationships that could have appeared to influence the work reported in this paper.

Acknowledgements

We thank: F. Bassange, J. Temu, A. Tibaijuka, and E. Bwasiri (Tanzania Antiquities Unit), E. Mshui and E. Mbede (University of Dar es Salaam), and the Tanzania Commission for Science and Technology; T. Orr for assistance in collecting field data; H. Huang and Y. Hu for laboratory assistance with analytical procedures; L. Kasenagala for field logistics and all RRBP field team members from 2002-present. We also thank Tyrone Rooney, an anonymous reviewer, and Editor-in-Chief Catherine Chauvel for their detailed reviews of this manuscript. This work was supported by the United States National Science Foundation grants (EAR-0617561, BCS-1638796 & EAR-1349825), the James Cook University post-graduate scholarship, the Economic Geology Research Centre (EGRU), and the W.R. Lacy Scholarship.

Appendix A. Supplementary data

Supplementary data to this article can be found online at https://doi.org/10.1016/j.chemgeo.2022.121040.

References

Bagley, B., Nyblade, A.A., 2013. Seismic anisotropy in eastern Africa, mantle flow, and the African superplume. Geophys. Res. Lett. 40, 1500–1505.
Begg, G.C., Griffin, W.L., Natapov, L.M., O'Reilly, S.Y., Grand, S.P., O'Neill, C.J., Hronsky, J.M.A., et al., 2009. The lithospheric architecture of Africa: Seismic tomography, mantle petrology, and tectonic evolution. Geosphere 5, 23–50.
Bell, K., Tilton, G., 2001. Nd, Pb and Sr isotopic compositions of East African carbonatites: evidence for mantle mixing and plume inhomogeneity. J. Petrol. 42, 1927–1945.
Borrego, D., Nyblade, A.A., Accardo, N.J., Gaherty, J.B., Ebinger, C.J., Shillington, D.J., Chindandali, P.R., Mbogoni, G., Ferdinand, R.W., Mulibo, G., O'Donnell, J.P., 2018.

Crustal structure surrounding the northern Malawi rift and beneath the Rungwe Volcanic Province, East Africa. Geophys. J. Int. 215, 1410–1426.
Castillo, P.R., Hilton, D.R., Halldórsson, S.A., 2014. Trace element and Sr-Nd-Pb isotope geochemistry of Rungwe Volcanic Province, Tanzania: implications for a superplume source for East Africa Rift magmatism. Front. Earth Sci. 2, 21.
Chakrabarti, R., Basu, A.R., Santo, A.P., Tedesco, D., Vaselli, O., 2009. Isotopic and geochemical evidence for a heterogeneous mantle plume origin of the Virunga volcanics, Western rift, East African Rift system. Chem. Geol. 259, 273–289.
Chorowicz, J., 2005. The east African rift system. J. Afr. Earth Sci. 43, 379–410.
Dawson, J., 1992. Neogene tectonics and volcanicity in the North Tanzania sector of the Gregory Rift Valley: contrasts with the Kenya sector. Tectonophys 204, 81–92.
Delvaux, D., Kervyn, F., Macheyeki, A., Temu, E., 2012. Geodynamic significance of the TRM segment in the East African Rift (W-Tanzania): active tectonics and paleostress in the Ufipa plateau and Rukwa basin. J. Struct. Geol. 37, 161–180.
Ebinger, C.J., 1989. Tectonic development of the western branch of the East African rift system. Geol. Soc. Am. Bull. 101, 885–903.
Ebinger, C.J., Sleep, N., 1998. Cenozoic magmatism throughout East Africa resulting from impact of a single plume. Nature 395, 788–791.
Ebinger, C.J., Deino, A.L., Drake, R., Tesha, A., 1989. Chronology of volcanism and rift basin propagation: Rungwe volcanic province, East Africa. J. Geophys. Res. Solid Earth 94, 15785–15803.
Fisher, C.M., McFarlane, C.R.M., Hanchar, J.M., Schmitz, M.D., Sylvester, P.J., Lam, R., Longerich, H.P., 2011. Sm-Nd isotope systematics by laser ablation-multicollector-inductively coupled plasma mass spectrometry: Methods and potential natural and synthetic reference materials. Chem. Geol. 284, 1–20.
Foley, S., Link, K., Tiberindwa, J., Barifaijo, E., 2012. Patterns and origin of igneous activity around the Tanzanian craton. J. Afr. Earth Sci. 62, 1–18.
Fontijn, K., Delvaux, D., Ernst, G.G., Kervyn, M., Mbede, E., Jacobs, P., 2010. Tectonic control over active volcanism at a range of scales: Case of the Rungwe Volcanic Province, SW Tanzania; and hazard implications. J. Afr. Earth Sci. 58, 764–777.
Fontijn, K., Williamson, D., Mbede, E., Ernst, G.G., 2012. The Rungwe volcanic province, Tanzania–a volcanological review. J. Afr. Earth Sci. 63, 12–31.
Fritz, H., Tenczer, V., Hauzenberger, C.A., Wallbrecher, E., Hoinkes, G., Muhongo, S., Mogessie, A., 2005. Central Tanzanian tectonic map: a step forward to decipher Proterozoic structural events in the East African Orogen. Tect 24 (6).
Furman, T., 1995. Melting of metasomatized subcontinental lithosphere: undersaturated mafic lavas from Rungwe, Tanzania. Contrib. Mineral. Petrol. 122, 97–115.
Furman, T., 2007. Geochemistry of East African Rift basalts: an overview. J. Afr. Earth Sci. 48, 147–160.
Furman, T., Graham, D., 1994. Chemical and isotopic variations in volcanic rocks from the Rungwe Province: constraints on the development and scales of source heterogeneity beneath the African Western Rift. Mineral. Mag. 58, 297–298.
Furman, T., Graham, D., 1999. Erosion of lithospheric mantle beneath the East African Rift system: geochemical evidence from the Kivu volcanic province. In: Developments in Geotectonics. Elsevier, pp. 237–262.
Furman, T., Nelson, W.R., Elkins-Tanton, L.T., 2016. Evolution of the East African rift: Drip magmatism, lithospheric thinning and mafic volcanism. Geochim. Cosmochim. Acta 185, 418–434.
Gao, P., Zheng, Y.F., Zhao, Z.F., 2016. Experimental melts from crustal rocks: a lithochemical constraint on granite petrogenesis. Lithos 266, 133–157.
Grijalva, A., Nyblade, A.A., Homman, K., Accardo, N.J., Gaherty, J.B., Ebinger, C.J., Shillington, D.J., Chindandali, P.R., Mbogoni, G., Ferdinand, R.W., Mulibo, G., 2018. Seismic evidence for plume-and craton-influenced upper mantle structure beneath the northern Malawi rift and the Rungwe volcanic province, East Africa. Geochem. Geophys. Geosyst. 19, 3980–3994.
Halldórsson, S.A., Hilton, D.R., Scarsi, P., Abebe, T., Hopp, J., 2014. A common mantle plume source beneath the entire East African Rift System revealed by coupled helium-neon systematics. Geophys. Res. Lett. 41, 2304–2311.
Hammerli, J., Kemp, A., Spandler, C., 2014. Neodymium isotope equilibration during crustal metamorphism revealed by in situ microanalysis of REE-rich accessory minerals. Earth Planet. Sci. Lett. 392, 133–142.
Hauzenberger, C.A., Tenczer, V., Bauernhofer, A., Fritz, H., Klötzli, U., Košler, J., Wallbrecher, E., Muhongo, S., 2014. Termination of the southern Irumide belt in Tanzania: zircon U/Pb geochronology. Precambrian Res. 255, 144–162.
Hilbert-Wolf, H., Roberts, E., Downie, B., Mtelela, C., Stevens, N.J., O'Connor, P., 2017. Application of U–Pb detrital zircon geochronology to drill cuttings for age control in hydrocarbon exploration wells: A case study from the Rukwa Rift Basin, Tanzania. AAPG Bull. 101, 143–159.
Hopper, E., Gaherty, J.B., Shillington, D.J., Accardo, N.J., Nyblade, A.A., Holtzman, B.K., Havlin, C., Scholz, C.A., Chindandali, P.R., Ferdinand, R.W., Mulibo, G.D., 2020. Preferential localized thinning of lithospheric mantle in the melt-poor Malawi Rift. Nat. Geosci. 13, 584–589.
Hudgins, T.R., Mukasa, S.B., Simon, A.C., Moore, G., Barifaijo, E., 2015. Melt inclusion evidence for CO_2-rich melts beneath the western branch of the East African Rift: implications for long-term storage of volatiles in the deep lithospheric mantle. Contrib. Mineral. Petrol. 169, 1–18.
Ivanov, A.V., Rasskazov, S.V., Boven, A., Andre, L., Maslovskaya, M.N., Temu, E.B., 1998. Late Cenozoic alkaline-ultrabasic and alkaline basanite magmatism of the Rungwe Province, Tanzania. Petrol 6, 208–229.
Kampunzu, A., Lubala, R., 2012. Magmatism in Extensional Structural Settings: The Phanerozoic African Plate. Springer Science & Business Media.
Kemp, A.I.S., Hawkesworth, C.J., Collins, W.J., Gray, C.M., Blevin, P.L., 2009. Isotopic evidence for rapid continental growth in an extensional accretionary orogen: the Tasmanides, eastern Australia. Earth Planet. Sci. Lett. 284, 455–466.
Kilembe, E.A., Rosendahl, B.R., 1992. Structure and stratigraphy of the Rukwa rift. Tectonophys 209, 143–158.
Lawrence, L., 2021. Geochemistry and Origin of Explosive Alkaline Volcanism in the Early Rukwa Rift, Southwestern Tanzania. PhD thesis. James Cook University, Townsville Queensland.
Lawrence, L., Spandler, C., Roberts, E., Hilbert-Wolf, H., 2021. Mineralogy and origin of the alkaline Nsungwe Formation tuffs of the Rukwa Rift Basin, southwestern Tanzania. Lithos 105885.
Liew, T.C., Hofmann, A.W., 1988. Precambrian crustal components, plutonic associations, plate environment of the Hercynian Fold Belt of Central Europe: indications from a Nd and Sr isotopic study. Contrib. Mineral. Petrol. 98, 129–138.
MacDonald, R., Rogers, N., Fitton, J., Black, S., Smith, M., 2001. Plume–lithosphere interactions in the generation of the basalts of the Kenya Rift, East Africa. J. Petrol. 42, 877–900.
Manya, S., 2011. Nd-isotopic mapping of the Archaean–Proterozoic boundary in southwestern Tanzania: Implication for the size of the Archaean Tanzania Craton. Gondwana Res. 20, 325–334.
Mesko, G.T., 2020. Magmatism at the Southern End of the East African Rift System: Origin and Role during Early Stage Rifting. PhD thesis. Columbia University, New York.
Morisset, N., 1993. Stable Isotope and Radioisotope Geochemistry of the Panda Hill Carbonatite, Tanzania. M.Sc. thesis. Carleton University, Ottawa, Ontario.
Morley, C., Cunningham, S., Harper, R., Wescott, W.A., 1992a. Geology and geophysics of the Rukwa rift, East Africa. Tectonics 11, 69–81.
Morley, C.K., Wescott, W.A., Stone, D.M., Harper, R.M., Wigger, S.T., Karanja, F.M., 1992b. Tectonic evolution of the northern Kenyan Rift. J. Geol. Soc. 149, 333–348.
Mtelela, C., Roberts, E.M., Downie, R., Hendrix, M.S., 2016. Interplay of structural, climatic, and volcanic controls on late quaternary lacustrine–deltaic sedimentation patterns in the Western Branch of the East African Rift System, Rukwa Rift Basin, Tanzania. J. Sediment. Res. 86, 1179–1207.
Mtelela, C., Roberts, E.M., Hilbert-Wolf, H.L., Downie, R., Hendrix, M.S., O'Connor, P.M., Stevens, N.J., 2017. Sedimentology and paleoenvironments of a new fossiliferous late Miocene-Pliocene sedimentary succession in the Rukwa Rift Basin, Tanzania. J. Afr. Earth Sci. 129, 260–281.
Mulaya, E., Gluyas, J., McCaffrey, K., Phillips, T., Ballentine, C., 2021. Structural geometry and evolution of the Rukwa Rift Basin, Tanzania: implications for helium potential. Basin Res. https://doi.org/10.1111/bre.12646.
Njinju, E.A., Atekwana, E.A., Stamps, D.S., Abdelsalam, M.G., Atekwana, E.A., Mickus, K. L., Fishwick, S., Kolawole, F., Rajaonarison, T.A., Nyalugwe, V.N., 2019. Lithospheric structure of the Malawi Rift: implications for magma-poor rifting processes. Tectonics 38, 3835–3853.
Nyblade, A.A., 2011. The upper-mantle low-velocity anomaly beneath Ethiopia, Kenya, and Tanzania: Constraints on the origin of the African superswell in eastern Africa and plate versus plume models of mantle dynamics. Geol. Soc. Am. Spec. Pap. 478, 37–50.
O'Connor, J., Stoffers, P., van den Bogaard, P., McWilliams, M., 1999. First seamount age evidence for significantly slower African plate motion since 19 to 30 Ma. Earth Planet. Sci. Lett. 171, 575–589.
Pik, R., Marty, B., Carignan, J., Yirgu, G., Ayalew, T., 2008. Timing of East African Rift development in southern Ethiopia: implication for mantle plume activity and evolution of topography. Geology 36, 167–170.
Rasskazov, S.V., Logachev, N.A., Ivanov, A.V., Boven, A.A., Maslovskaya, M.N., Saranina, E.V., Brandt, I.S., Brandt, S.B., 2003. A magmatic episode in the Western Rift of East Africa (19-17 Ma). Geol. Geofiz. 44, 317–324.
Ring, U., 2014. The east African Rift System. Austrian J Earth Sci 107, 132–146.
Roberts, E.M., O'Connor, P.M., Stevens, N.J., Gottfried, M.D., Jinnah, Z.A., Ngasala, S., Choh, A.M., Armstrong, R.A., 2010. Sedimentology and depositional environments of the Red Sandstone Group, Rukwa Rift Basin, southwestern Tanzania: New insight into cretaceous and Paleogene terrestrial ecosystems and tectonics in sub-equatorial Africa. J. Afr. Earth Sci. 57, 179–212.
Roberts, E.M., Stevens, N.J., O'Connor, P.M., Dirks, P.H.G.M., Gottfried, M.D., Clyde, W. C., Armstrong, R.A., Kemp, A.I.S., Hemming, S., 2012. Initiation of the western branch of the East African Rift coeval with the eastern branch. Nat. Geosci. 5, 289.
Rogers, N., James, D., Kelley, S., De Mulder, M., 1998. The generation of potassic lavas from the eastern Virunga Province, Rwanda. J. Petrol. 39, 1223–1247.
Rooney, T.O., 2017. The Cenozoic magmatism of East-Africa: Part I—flood basalts and pulsed magmatism. Lithos 286, 264–301.
Rooney, T.O., 2020. The Cenozoic magmatism of East Africa: part V–magma sources and processes in the East African Rift. Lithos 360, 105296.
Rooney, T.O., Hanan, B.B., Graham, D.W., Furman, T., Blichert-Toft, J., Schilling, J.G., 2012. Upper mantle pollution during Afar plume–continental rift interaction. J. Petrol. 53, 365–389.
Rooney, T.O., Nelson, W.R., Dosso, L., Furman, T., Hanan, B., 2014. The role of continental lithosphere metasomes in the production of HIMU-like magmatism on the northeast African and Arabian plates. Geology 42, 419–422.
Rosenthal, A., Foley, S., Pearson, D.G., Nowell, G.M., Tappe, S., 2009. Petrogenesis of strongly alkaline primitive volcanic rocks at the propagating tip of the western branch of the East African Rift. Earth Planet. Sci. Lett. 284, 236–248.
Spandler, C., Hammerli, J., Sha, P., Hilbert-Wolf, H., Hu, Y., Roberts, E., Schmitz, M., 2016. MKED1: a new titanite standard for in situ analysis of Sm–Nd isotopes and U–Pb geochronology. Chem. Geol. 425, 110–126.
Spandler, C., Hammerli, J., Pirard, C., 2018. Neodymium isotope disequilibria in subducted sediments, and potential consequences for subduction-zone recycling. Geology 46, 815–818.
Stevens, N.J., Seiffert, E.R., O'Connor, P.M., Roberts, E.M., Schmitz, M.D., Krause, C., Gorscak, E., Ngasala, S., Hieronymus, T.L., Temu, J., 2013. Palaeontological evidence for an Oligocene divergence between Old World monkeys and apes. Nature 497, 611.

Sun, K., Zhao, Z., Zhang, L., Qiu, L., Liu, X., He, S., Ren, J., Ye, L., Cui, Y., 2021. Geochronology, Petrography and Sr-Nd-Hf isotopes of Mbalizi carbonatite, southwestern Tanzania. J. Afr. Earth Sci. 104308.

Tappe, S., Foley, S.F., Stracke, A., Romer, R.L., Kjarsgaard, B.A., Heaman, L.M., Joyce, N., 2007. Craton reactivation on the Labrador Sea margins: $^{40}Ar/^{39}Ar$ age and Sr–Nd–Hf–Pb isotope constraints from alkaline and carbonatite intrusives. Earth Planet. Sci. Lett. 256, 433–454.

Tepp, G., Ebinger, C.J., Zal, H., Gallacher, R., Accardo, N., Shillington, D.J., Gaherty, J., Keir, D., Nyblade, A.A., Mbogoni, G.J., Chindandali, P.R.N., 2018. Seismic anisotropy of the upper mantle below the Western rift, East Africa. J. Geophys. Res. Solid Earth 123, 5644–5660.

Wade, B.P., Barovich, K.M., Hand, M., Scrimgeour, I.R., Close, D.F., 2006. Evidence for early Mesoproterozoic arc magmatism in the Musgrave Block, Central Australia: Implications for Proterozoic crustal growth and tectonic reconstructions of Australia. J. Geol. 114, 43–63.

Walter, B.F., Giebel, R.J., Steele-MacInnis, M., Marks, M.A., Kolb, J., Markl, G., 2021. Fluids associated with carbonatitic magmatism: a critical review and implications for carbonatite magma ascent. Earth Sci. Rev. 215, 103509.

Woodhead, J.D., Hergt, J.M., 2005. A preliminary appraisal of seven natural zircon reference materials for in situ Hf isotope determination. Geostand. Geoanal. Res. 29, 183–195.

Yang, Y.H., Wu, F.Y., Yang, J.H., Chew, D.M., Xie, L.W., Chu, Z.Y., et al., 2014. Sr and Nd isotopic compositions of apatite reference materials used in U–Th–Pb geochronology. Chem. Geol. 385, 35–55.

Yaxley, G.M., Anenburg, M., Tappe, S., Decree, S., Guzmics, T., 2022. Carbonatites: classification, sources, evolution, and emplacement. Annu. Rev. Earth Planet. Sci. 50.

Yoshida, M., Windley, B.F., Dasgupta, S., 2003. Proterozoic East Gondwana: Supercontinent Assembly and Breakup. Geological Society of London.